MDPI

Article

Wind Turbine Blade-Tip Optimization: A Systemic Computational Approach

Panagiotis Zouboulis [1], Elias P. Koumoulos [2] and Anna Karatza [1,*]

[1] BIOG3D P.C., Technological & Cultural Park of Lavrion, 1 Lavriou Ave., 19500 Lavrion, Greece
[2] IRES—Innovation in Research and Engineering Solutions, Rue Koningin Astridlaan 59B, 1780 Wemmel, Belgium
[*] Correspondence: akaratza@biog3d.gr; Tel.: +30-2292022512

Abstract: Curved bladelets on wind turbine blades play an important role in improving the performance and efficiency of wind turbines. Implementing such features on the tip of wind turbine blades can improve their overall aerodynamic characteristics by reducing turbulence and loading without hindering lift generation and overall efficiency, thus leading to increased energy capture and reduced costs over the life of the turbine. Subjecting the integrated blade tip to optimization procedures can maximize its beneficial contribution to the assembly in general. Within this context, a systemic workflow is proposed for the optimization of a curved bladelet implemented on a wind turbine blade. The approach receives input in the form of an initial tip geometry and performs improvements in two distinct stages. Firstly, shape optimization is performed directly on the outer shape to enhance its aerodynamic properties. Subsequently, the topology of its interior structure is refined to decrease its mass while retaining its improved airflow characteristics. The proposed workflow aims to approach blade tip optimization holistically, both in terms of aerodynamic performance and structural capabilities; is computationally validated via fluid dynamics studies and finite element analysis to evaluate the performance augmentation achieved through it; and is further coupled with additive manufacturing for the production of prototype parts, benefiting from the manufacturing flexibility offered by digital fabrication technologies. The optimized bladelet model presented an approximate 30% improvement in the torque generated on it, while maintaining only 70% of its original mass, effectively contributing to a 0.81% increase to the total torque generated by the blade, consequently confirming the effectiveness of the proposed methodology.

Keywords: wind energy; bladelet; blade tip; CFD; optimization; topology; 3D printing; additive manufacturing

1. Introduction

Wind energy is one of the most exploited renewable energy sources, measuring a total global wind power capacity of up to 837 GW in 2022, with projections showing an annual increase at this value of approximately 9% [1]. Costs to manufacture and deploy wind turbines remain a significant investment, which further escalates by taking into consideration wind turbine maintenance costs and their finite lifecycle [2]. Within the scope of designing a wind turbine, the main objective is to generate maximum effective power while maintaining the lowest possible production costs. The power produced by a wind turbine depends primarily on the aerodynamic properties of its blades. The cost of manufacturing the blades for a wind turbine, and therefore for the entire wind turbine, depends on the materials used for its production as well as its internal geometric structure, aiming for minimum compliance and mass. By selecting the optimal material and geometric properties of the wind turbine blade, it is possible to reduce the costs of making the entire wind turbine [3]. The process of developing components, products and structures with the least possible amount of mass within the framework of certain predefined constraints,

related to their purpose and operating conditions, follows a specific design pattern and is traditionally named "design for lightweight" [4].

In order to balance the cost of wind energy plants without compromising overall efficiency, wind turbine technology improvements are necessary, calling for larger rotor diameters and higher hub-heights, allowing for larger harvesting rates per turbine from plant sites [5]. One important focus of this improvement targets the development of high performing and cost-efficient wind blades, through design optimization [6].

Wind blade design optimization can be performed in three distinct stages. The first stage includes the integration of supportive features on the tip of the blades to improve its aerodynamic properties [7]. Implementation of curved bladelet tips on wind turbine blades can potentially improve performance, increase efficiency and contribute to the overall energy output without significant alteration of the diameter of the turbine rotor [8–10]. Secondly, Shape Optimization (SO) of the external shape of the blade is considered. By performing targeted improvements on the base form of the blade airfoil, the airflow around the blade is facilitated, thus leading to higher generated torque values under the same operating conditions [11]. Finally, further enhancement can also be achieved by means of Topology Optimization (TO) by reducing the total material expended in the internal structure of the blade without compromising its structural integrity [12]. These steps, in combination with state-of-the-art manufacturing technologies, such as additive manufacturing and the application of advanced materials, such as reinforced composites as well as advanced polymers capable of withstanding high loads in least material condition leads to optimized blade performances while fabrication costs, are simultaneously contained due to material savings [13]. Combining the geometry optimization with 3D printing technologies allows for the rapid fabrication of optimized geometries taking advantage of an extended manufacturing flexibility that additive manufacturing offers, especially in the case of internal organic structural features produced through the optimization algorithms [14].

Focusing the optimization process around the integrated bladelet presents compelling interest as the additional feature exhibits the most volatile behavior due to its geometry and position on the tip of the blade [10]. Several approaches have been realized so far. Reddy et al. pointed out the limitations in available literature, with regard to the design of curved bladelets in rotating bladed mechanisms, while applying a computational optimization approach on the tip to demonstrate the benefits of optimization [7]. Sessarego et al. employed neural networks leading to an approximate 1% increase on the generated power though such models require training data and exhibit significant computational costs [15]. Madsen et al. implemented a CFD-based method to develop improved curved tips in an attempt to establish a high-fidelity framework whose paucity their investigation identified [16].

Although various studies have addressed the topic of bladelet optimization in terms of aerodynamic behavior as well as regarding the internal topology of the component, there appears to be a scarcity of investigations that engage with both operations in a single multi-step, single-system approach. This current study aims to convey a holistic workflow developed and followed for the optimization of an integrated bladelet tip of the IEA 15MW reference turbine blade, both regarding the external shape optimization and internal structure aiming to compensate for this paucity.

2. Materials and Methods

In order to optimize the tip of the wing turbine blade, a two-stage approach was developed. At first, the external aerodynamic characteristics of the tip were modified by employing a shape optimization algorithm aiming to maximize the generated torque without major changes on the overall length of the blade and the implemented blended curved tip [7]. Subsequently, the internal structure of the blade underwent computational topology optimization study towards an improved geometry aiming for maximum compliance at least material condition [13]. During this step, the design flexibility offered by AM was taken into consideration, presenting a significant contribution towards the manufacturabil-

ity of the optimized component [14]. The overall roadmap of the aforementioned approach is presented in Figure 1.
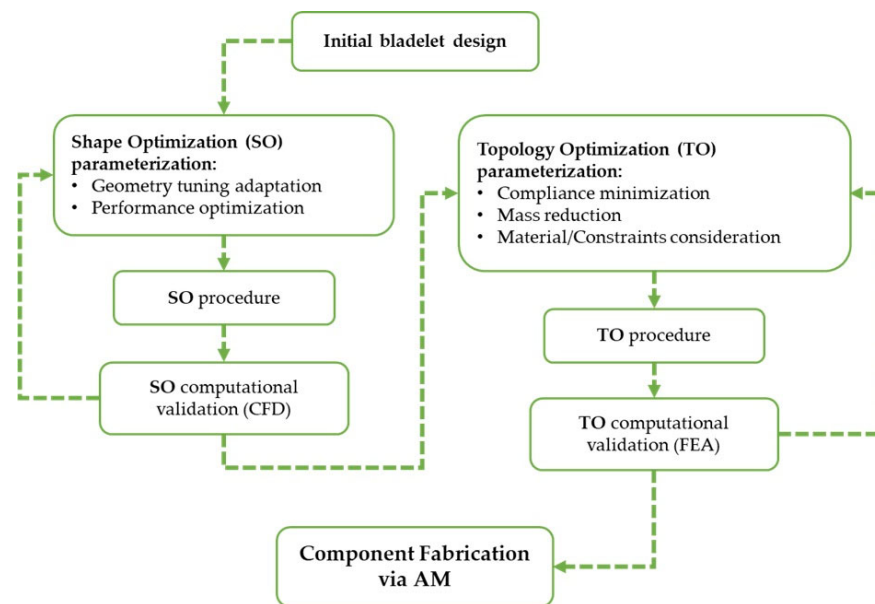

Figure 1. Bladelet optimization strategy overall schematic roadmap.

2.1. Shape Optimization

Shape design optimization is a vital part of the product design workflow, which approaches the design process in a systemic manner, investigating the effect of all input and output parameters of the given system and adjusting each accordingly with the scope of producing the best possible solution for a given design problem [17,18].

The adjoint solver methodology is exploited as a shape optimization technique, which makes use of a specialized mathematical tool that provides detailed sensitivity analysis regarding the performance of a fluid system with solid elements that is subjected to specific boundary conditions [19]. The adjoint optimization method considers the computational flow solution $\underline{q}$ and defines the problem inputs in the form of a vector $\underline{c}$. The quantity of interest is $J\left(\underline{q}(\underline{c}); \underline{c}\right)$, and the residuals of the Navier Stokes equations are $R_i\left(\underline{q}(\underline{c}); \underline{c}\right) = 0$. By defining the Lagrangian L with the vector of Lagrange multipliers $\overline{\underline{q}}^T$ (the adjoint solution variable), the following equation takes form:

$$\frac{dJ}{d\underline{c}} = \frac{d\underline{q}}{d\underline{c}}\left(\frac{dJ}{d\underline{q}} + \overline{\underline{q}}^T \frac{\theta R}{\theta \underline{q}}\right) + \frac{\theta J}{\theta \underline{c}} + \overline{\underline{q}}^T \frac{\theta R}{\theta \underline{c}}. \qquad (1)$$

By choosing a $\overline{\underline{q}}^T$ such that:

$$\frac{\theta J}{\theta \underline{c}} + \overline{\underline{q}}^T \frac{\theta R}{\theta \underline{c}} = 0 \rightarrow \overline{\underline{q}}^T \left[\frac{\theta R}{\theta \underline{c}}\right]^T = -\left[\frac{\theta J}{\theta \underline{c}}\right]^T, \qquad (2)$$

the problem is reduced to linear form:

$$\frac{dJ}{d\underline{c}} = \frac{\theta J}{\theta \underline{c}} + \overline{\underline{q}}^T \frac{\theta R}{\theta \underline{c}}, \qquad (3)$$

where the left-hand side indicates the adjoint sensitivities. The sensitivity equation is evaluated at each given mesh node in the CFD model. For shape sensitivity, the input vector $\underline{c}$ is considered as the (x, y, z) coordinates of every node in the model. In the same equation, the $\frac{\theta J}{\theta \underline{c}}$ factor is the change in J value due to changes in the (x, y, z) coordinates,

and $\overline{q}^T \frac{\theta R}{\theta \underline{c}}$ refers to the changes induced in J due to the sensitivity of the flow solution at given nodes locations, depending on the adjoint solution itself. Both parameters are calculated using expressions deriving from the observable definitions and the discretized computational model equations. Thus, by solving the adjoint problem:

$$\overline{\underline{q}}^T \left[\frac{\theta R}{\theta \underline{c}} \right]^T = - \left[\frac{\theta J}{\theta \underline{c}} \right]^T, \tag{4}$$

the computation of the shape derivative takes place in even large-scale optimization cycles. This solution is carried out as follows. The adjoint residuals are calculated using the formula:

$$\overline{R} = \frac{\theta J}{\theta q_j} - \frac{\theta R_i}{\theta q_j} \overline{q}_i. \tag{5}$$

The correction to the solution is determined:

$$M \Delta \overline{q}_i = \frac{\theta J}{\theta q_j} - \frac{\theta R_i}{\theta q_j} \overline{q}_i = \overline{R}. \tag{6}$$

The adjoint equations are updated using the corrected vector:

$$\overline{q}_i = \overline{q}_i + a_i \Delta \overline{q}_i. \tag{7}$$

This iterative process repeats until the specified threshold is reached or the predefined maximum number of iterations is complete. The aim of this work is to extend the scope of a CFD study by extracting data with regard to the system's sensitivity against geometrical changes by computing the derivative of engineering quantities, taking into consideration every system input, including flow geometry [20]. This capability is utilized to realize intelligent design modifications for shape optimization of any geometric feature in the defined computational domain and further identify the optimal shape for given operating conditions, deriving from a baseline CFD flow calculation. As such, no model parameterization is necessary, making it a suitable candidate for intricate non-parametric geometries [21]. At first, the study makes use of user-defined relevant observables. Various scalar quantities of interest can act as observables, indicatively forces exerted on the component under investigation, flow parameters and geometric features. Either a continuous or discrete solver is selected, depending on the case, with the first option focusing on speed and memory efficiency and the second achieving higher accuracy by increasing the computational cost. Subsequently, accordingly tuned controls for the optimization procedure are utilized, aiming to produce a stable and robust calculation. Predetermined residuals with suitable convergence values balance precision and computational cost. After the completion of the aforementioned steps, the solver performs the calculation in order to identify the system sensitivities, essentially predicting how geometry alterations would affect the performance of the part. Optimization cycles are suggested to be carried out in short cycles, with incremental sets of moderate or small improvement each time, up to 10% of the initial value, as larger increments pose risk of causing solution overshoot and potentially guiding the solver to converge on suboptimal results. The described workflow is presented schematically in Figure 2. Limiting the optimization area locally to the features of interest, such as the curved tip of the wind turbine blade in this specific scenario (Figure 3), can further aid in minimizing the computational cost and isolating specific areas that require improvement while preserving others. A stabilization scheme was implemented to support the concurrence of the study within the preset number of iterations by monitoring local flow rate and air velocity residual value convergence around the tip. The solver was indicatively set to a maximum of 1000 calculation iterations, and the residual convergence was set at 10^{-5} for increased accuracy over the default values of 10^{-3}.
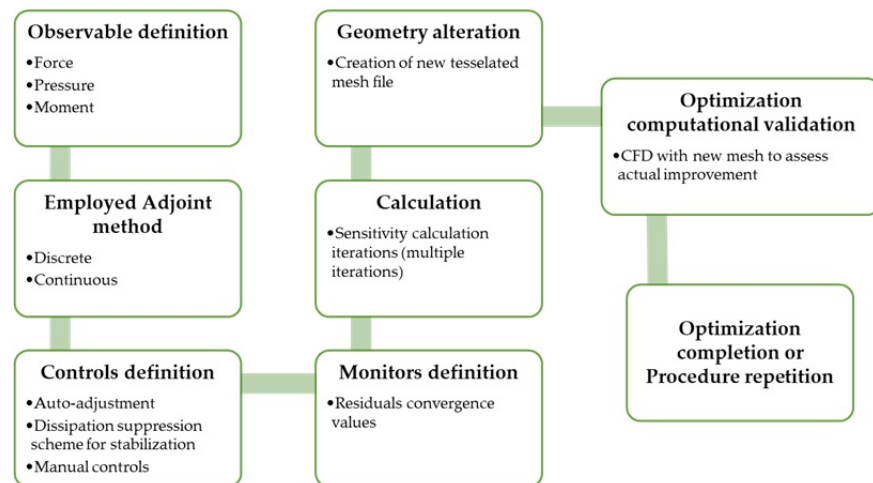
Figure 2. Adjoint Shape optimization specific workflow schematic.
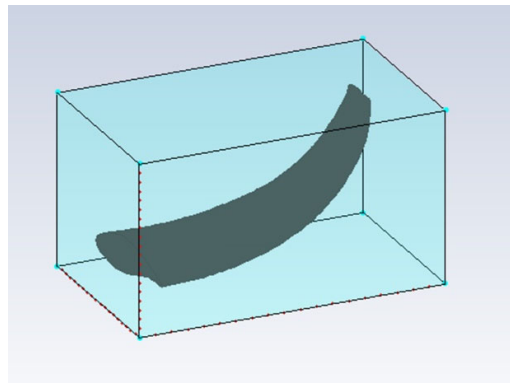

Figure 3. Shape optimization region definition.

After the completion of an appropriate number of calculation rounds, the user is able to carry out geometry adjustments, based on the calculation results, and extract the updated, potentially optimized geometry. This geometry has to undergo further simulations to validate the actual improvement.

The simulation scenario that was carried out as part of this optimization study to produce initial and post optimization performance results assumed constant rated wind velocity and rotor speed, set at 8.56 m/s and 6.22 rpm, respectively, in an indicative scenario aiming to support the two stage optimization workflow. A single blade of a three-blade rotor with a 240 m total diameter was examined, considering the symmetry of the rotor's layout, with a $-4°$ precone angle. The study utilized a finite conical mesh of tetrahedral elements (Figure 4), with a maximum element size of 24 m at the domain that adapted to smaller values near the Body of Interest (BOI), maintaining a steady size of 1.8 m around the blade and reaching down to 0.008 m near intricate features, such as the trailing edge of the blade. The element size values were selected through a mesh independence study, undergoing 4 consecutive refinement steps.
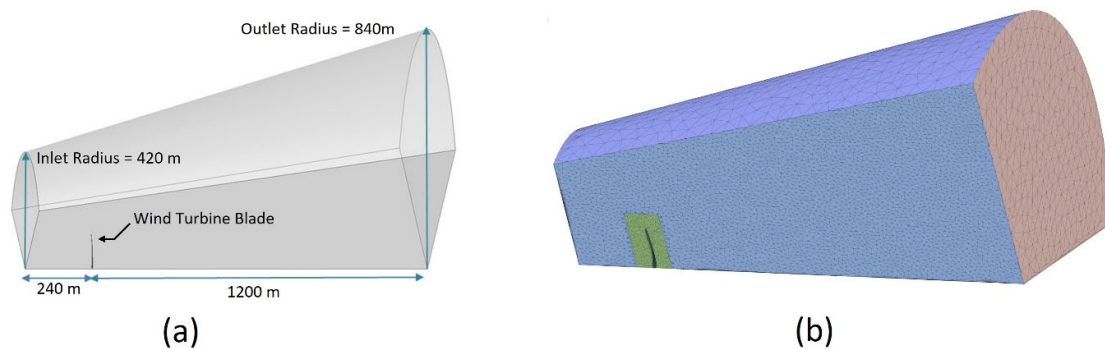
Figure 4. (**a**) CFD conical domain and (**b**) mesh domain representation for the CFD simulation.

The CFD study furthermore utilized a Shear Stress Transfer (SST) k-ω turbulence model to capture turbulent flows due to expected Reynolds numbers up to 2×10^6, considering the geometric and operating characteristics of the wind turbine under investigation. The studies were carried out in Ansys Fluent 2021 R1, employing time-dependent Reynolds Averaged Navier Stokes (RANS) equations [22]. The accuracy and reliability of the model was verified through comparison of the values for the tip speed and power coefficient. Whereas the tip speed remained within 1% of the nominal design value during every mesh refinement step, the difference between rated and calculated power coefficient decreased from 30.4% to 19.6% after the 4th refinement step. Further refinement of the mesh was not made possible at this point due to computational limitations.

2.2. Topology Optimization

Topology optimization (TO) is employed to achieve material reduction, essential for structural applications, where weight reduction is of the essence, and the quality and robustness of the structure may also require enhancement or preservation to a certain degree. It takes into consideration the material and operating conditions of the designed component in order to produce the most efficient geometry that meets its requirements, also meeting manufacturing constraints [23]. TO increases the design flexibility, as well as shortens the design process, and presents the potential to decrease lead times in product development, although it is a generally time intensive, iterative computational procedure [24].

One of the most widely employed algorithms to perform topology optimization is the Solid Isotropic Material with Penalization method (SIMP) [25]. Initially introduced by Bendsoe and Kikuchi in 1988, this methodology predicts the best available material distribution within a given design space, for predefined load cases, boundary conditions, manufacturing constraints and performance requirements and updated versions still widely employed in various optimization applications [26,27]. According to SIMP, the domain is discretized as a grid of finite elements named isotropic microstructures. These elements can be assigned a binary density value, either containing material (state 1) or being void (state 0). SIMP introduces a continuous relative density distribution varying between 1 and a specified minimum value ρ_{min}. A penalty factor p decreases the contribution of elements with intermediate densities to the total stiffness of the component. Using an iterative process, the optimization algorithm performs a sensitivity analysis to evaluate the impact of the variable material densities on the objective function to meet the objective (e.g., maximization of part stiffness) [28]. Mathematically, this sensitivity analysis is expressed as a derivative of the objective function with respect to the material densities:

$$\frac{dC}{d\rho_e} = -p(\rho_e)^{p-1}[u_e]^T[K_e][u_e], \tag{8}$$

where ρ_ε indicates the density vector value of the elements; K_e describes the stiffness matrix for the elements; and u_e is the nodal displacement vectors calculated during the iterative procedure [29]. The tools utilized within the context of this study employ the

SIMP combined with elements of an alternative technique named a level set method. Level set methods define the three-dimensional design space as an open bounded $D \in R^3$. The final, optimized shape is described by an additional set Ω, which is a subset of D. A level set function is defined such that:

$$\left\{ \begin{array}{l} (\chi) = 0 \leftrightarrow \chi \in \vartheta\Omega \\ \psi(\chi) < 0 \leftrightarrow \chi \in \Omega \\ \psi(\chi) > 0 \leftrightarrow \chi \in (D\backslash\overline{\Omega}) \end{array} \right\}, \tag{9}$$

The evolution of the shape Ω depends on the Hamilton Jacobi equation:

$$\frac{\vartheta\psi}{\vartheta t} - v|\nabla\psi| = 0, \tag{10}$$

where v is called the descent direction and is calculated by the optimizer in an attempt to morph the initial geometry towards a predefined goal [30,31].

The overall workflow for a structural TO study resembles the one described in the previous paragraph up to a degree and is depicted in Figure 5. An initial geometry is required, as well as information regarding material properties. Boundary conditions are specified, such as part mechanical or thermal loading and fixtures. Within the context of this specific approach, loading data is derived from the first stage, where the CFD analysis resulted in comprehensive pressure distribution profiles along the surface of the component (Figure 6). A design space in which shape changes can occur is also determined, allowing in a similar manner to external shape optimization to isolate regions of interest and potentially exclude sensitive areas, such as features with limited thickness, where material removal would lead to non-manufacturable parts or preserve vital segments of the initial geometry, such as bolt orifices or threads, necessary for assembly. A benchmarking Finite Element Analysis (FEA) is carried out to determine the behavior of the initial geometry. Following this step, an optimization goal must be user-defined, such as a mass reduction percentage or a compliance minimization target. The optimization algorithm follows this study, calculating the system sensitivities against shape alteration and material removal. A filtering software tool is then utilized to remove potential gray areas produced during this step, aiming for a clean solution geometry. An iterative optimization procedure is subsequently performed, incrementally calculating the shape alteration towards the predefined goals up to the point of convergence between the set and targeted values or until no further significant changes occur, signifying saturation. A validation FEA study confirms the effectiveness of the optimization, and the user receives the updated, enhanced geometry.
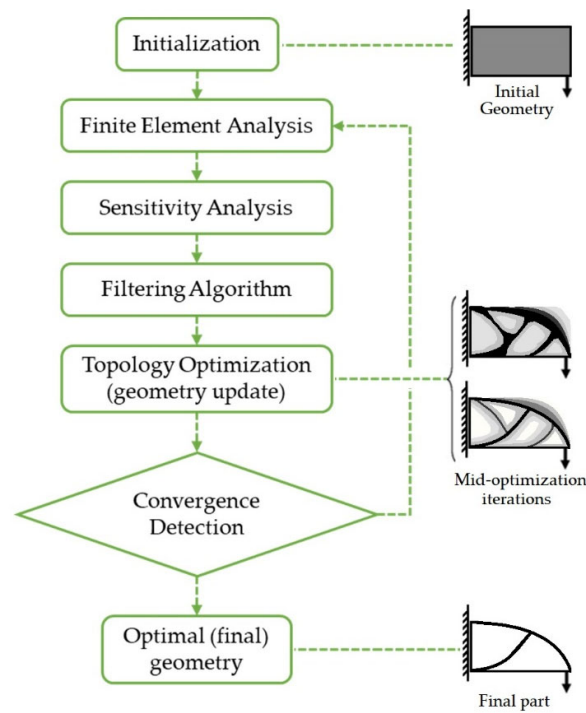
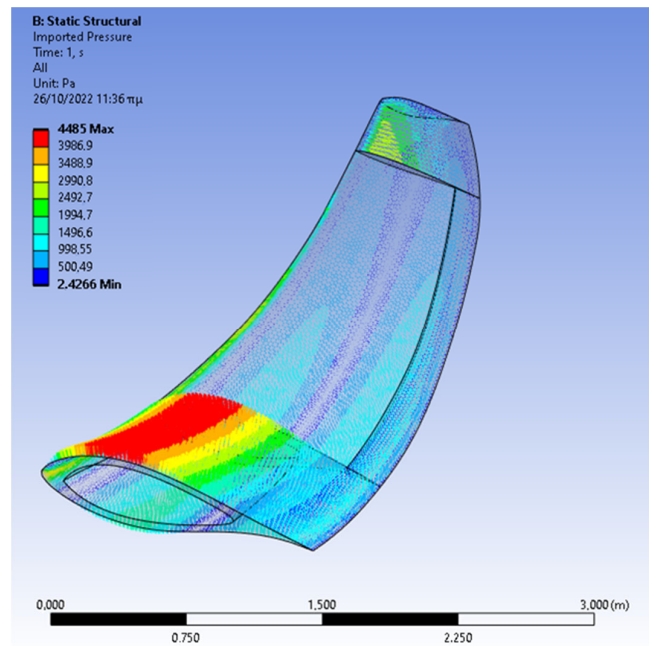**Figure 5.** Topology optimization specific schematic workflow.

Figure 6. Pressure distribution data generated from CFD study.

In order to determine the limitation point of the study, two distinct response constraints were set with regard to the amount of material to be removed and the strength of the resulting part. A 40% mass reduction limit was placed, and a safety factor of value 2 concerning the equivalent Von Mises stresses was developed on the component. The maximum number of optimization iterations was set at 20. This value is typically acceptable for a topology optimization analysis, with many instances usually converging in fewer. If no convergence is detected in the minimization of the compliance or the constraints set around mass removal and the safety factor, the process can continue for a larger user-defined number of iterations. A program-controlled solver type was selected as no specific

case constraints dictated for the application of an alternative method. The convergence accuracy was retained at the default value of 0.1%. Aiming to reduce computational time and avoid implications caused by implementing thin and small features in the study, the bladelet geometry was compartmentalized into 4 distinct sub-areas: the joining base; the main body; the trailing edge; and the thin tip of the bladelet (Figure 7). The region in which the solver will perform alterations and the areas to be excluded from the study are defined. In this case the hollowed-out base of the bladelet (Figure 7b) is excluded from the study, as much material has already been removed to facilitate attachment of the tip to the blade during assembly. Moreover, the trailing edge of the bladelet and the tip were also excluded due to their thinness, which would potentially increase the computational cost and produce parts with non-manufacturable thin features (Figure 7c,d). The external surface of the selected region for the optimization was also preserved so as to avoid removing material from the outer shell of the bladelet. The objective of the optimization was set in the form of minimization of the compliance of the given design throughout the material removal process.
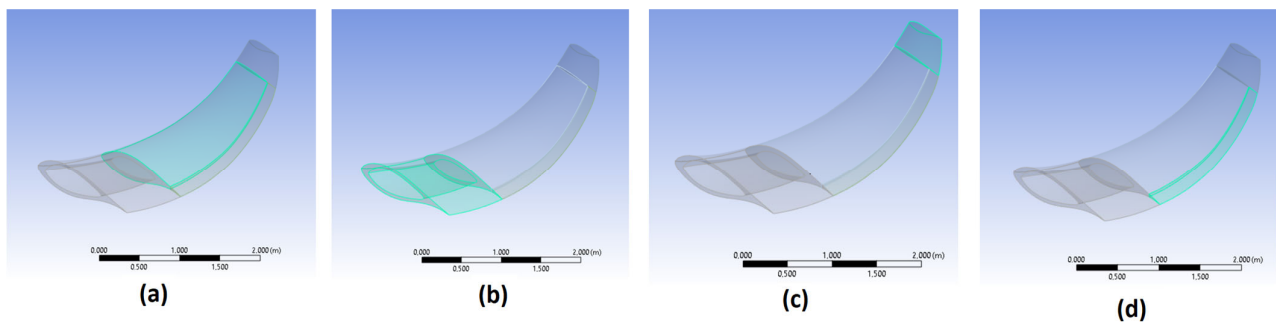

Figure 7. Geometry segmentation for TO facilitation. (**a**) Main body region, (**b**) hollow base for assembly, (**c**) bladelet tip region, (**d**) trailing edge region.

2.3. Validation through 3D Printing

Whereas structured industrial design usually consists of well-defined parametric features, shapes produced via shape and topology optimization are mostly comprised of free-form constituents, which are often challenging to manufacture using traditional, conventional fabrication techniques, such as CNC milling or composite fabric layup. Pairing optimization results with additive manufacturing technologies due to their ability to directly realize these complex, usually organic shapes can potentially provide the adopted methodology with a significantly higher degree of flexibility in comparison to conventional production workflows. In this current study, the development of a prototype for further experimentation and physical validation of the modeling process dictated the manufacturing of a scaled-down version of the optimized bladelet through 3D printing. The aforementioned investigation is not included in this publication. Vat Photopolymerization (VPP) 3D printing utilizes a light source, a vertically translating build plate, which is immersed in a transparent basin with liquid photopolymer resin. The light source is projected through an LCD screen, which acts as a masking layer, allowing for selective emission over the photopolymer, procedurally solidifying the resin in a layer-by-layer manner, leading to a 3D object (Figure 8). It is a 3D printing technology capable of attaining complex parts with intricate internal features and high surface quality. This technology further boasts a good degree of compatibility in terms of commercially available materials and high fabrication speed, compared to other AM technologies and compatibility with several translucent resins in order to fabricate partially transparent components, aiming to support the visualization of the internal configuration that occurred as a result of the TO process.
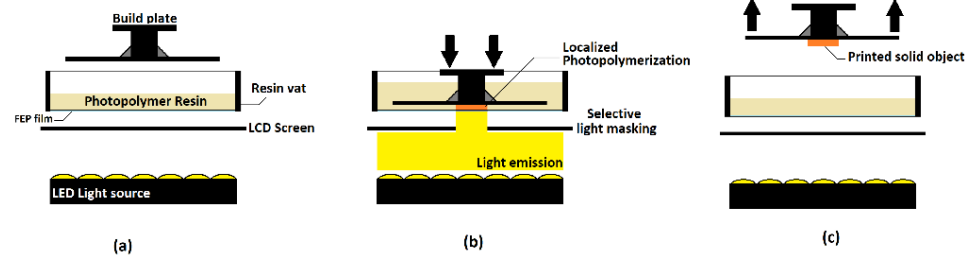
Figure 8. LCD VPP 3D printing schematic. (**a**) Overall configuration, (**b**) layer solidification step, (**c**) solid layer change step.

The demonstration of the methodology results presented in this study is carried out using a LC Magna VPP 3D printing unit, whose large build volume of $510 \times 270 \times 350$ mm designates it as a suitable match for the fabrication of scaled-down prototypes for wind turbine components. The material selected for printing was the Daylight Magna Draft Resin by Photocentric, due to its notable printing quality for rapid prototyping. This specific material displays notable mechanical properties, presenting high strength and stiffness, comparable to rigid engineering thermoplastics, such as Polyamide 12. 3D printing of this resin also results in translucent parts where any internal features are easily visible.

3. Results and Discussion

3.1. Shape Optimization Results

The adjoint shape optimization workflow was employed for 5 consecutive runs. During the first solution calculation, the observed tip-torque appeared to achieve a 9572.23 Nm increase, corresponding to an improvement of approximately 22% compared to the original output of the tip. In this case, the specified improvement increment had been set to a 20% increase in torque. Repeating the procedure for a total of 4 further design iterations resulted in an overall 33% gain, leading the generated torque on the bladelet at 57,577 Nm and 0.81% on the whole blade at 3,091,042 Nm. A validation CFD run confirmed this improvement returning accordingly torque values of 57,969 Nm on the tip of the blade and 3,192,793 Nm on the whole blade, respectively (Figure 9). Deviations between the calculated and simulated values appeared minimal, ranging from 0.68% on the tip to 3.2% on the whole blade. Therefore, after computational validation, an average generated torque increase of 30% was achieved on the tip of the blade via shape optimization and contributing to a 0.82% improvement on the whole blade.
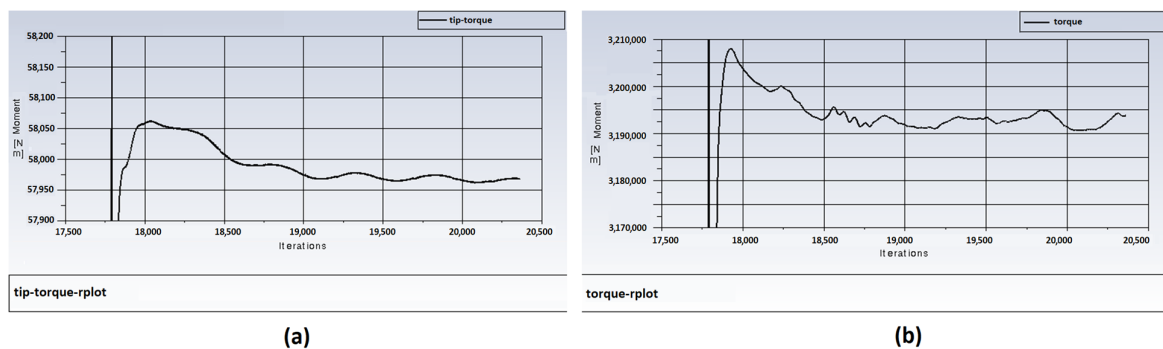

Figure 9. Torque value graphs against CFD iterations. (**a**) Torque generated on the tip of the blade, (**b**) torque generated on the whole blade.

In terms of shape alteration induced on the bladelet component through the shape optimization procedure, a detailed dimensional deviation color map is depicted in Figure 10. A general displacement of the airfoil camber line towards the upper surface can be observed, as well as a minor deflation of the upper surface near the leading edge. The trailing edge

near the tip of the bladelet appears to have twisted towards the upper side by a small degree. The numerical values of the observed dimensional deviations remain within the range of a few millimeters. Specifically, the maximum positive deviation (outward geometry inflation) observed was measured at 14.614 mm on the top surface of the bladelet, close to the trailing edge, at an approximate distance of 1 m from the component's base (approximately 2/3 of the reparametrized total length of the part). Accordingly, the maximum magnitude regarding negative deviation (inward geometry deflation) was observed on the upper surface towards the leading edge of the part at an approximate distance of 200 mm from the component's base, measuring at 27.623 mm.
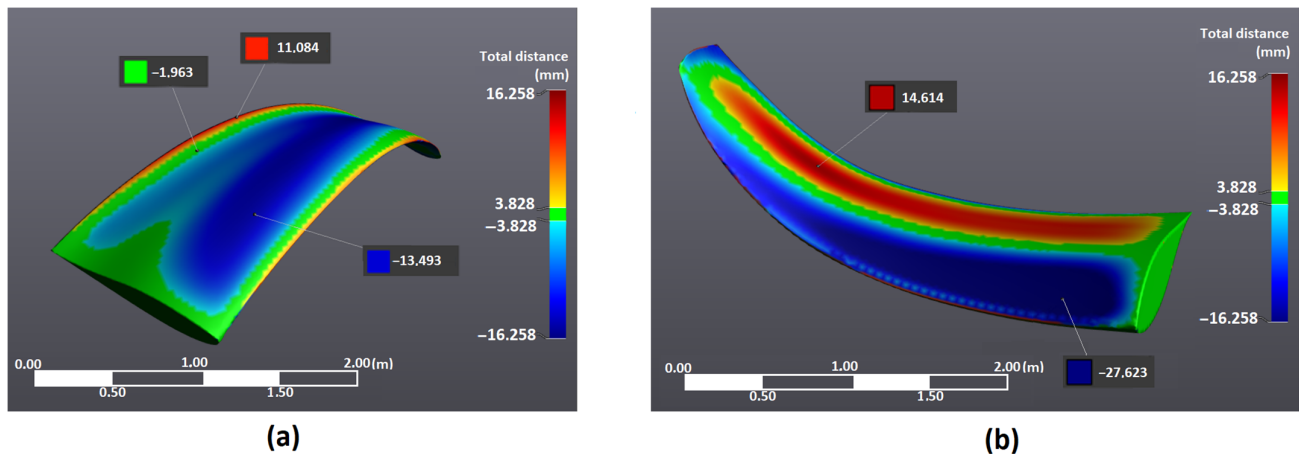

(a) **(b)**

Figure 10. Bladelet dimensional deviation [mm] after shape optimization. (**a**) Lower tip side, (**b**) upper tip side.

Deviations near the base of the bladelet were contained to a minimum, restricted under 3 mm so as to ensure proper matching of the tip to the blade during the assembly process of the prototype. This limitation was made possible during the region definition depicted in Figure 3. It is quite noteworthy that a targeted deformation in the order of a few millimeters on a component spanning approximately 3 m in length and 1.5 m in width can lead to a 30% performance enhancement. An additional optimization iteration for further investigation was conducted, producing marginal improvements, smaller than 1%, which was discarded as it did not justify the computational cost at this stage.

3.2. Topology Optimization Results

A total of 21 consecutive optimization iterations were required to achieve convergence considering the parametrization of the solver, the definition of the improvement criteria and corresponding constraints. A computation time of 44 min and 36 s was eventually necessary for the analysis to complete, after several reparameterization iteration attempts to provide the most appropriate configuration for the case at hand. As evident in Figure 11, a considerable amount of material was removed near the base of the bladelet component. A 30.26% mass reduction was achieved, compared to the original value. The removal of the material was focused on the first two-thirds of the total length of the model starting from its base. Moving towards the tip and the trailing edge, no material was removed from these two areas, as the low thickness would not be able to result in a manufacturable component. The updated internal structure appeared highly organic in nature and the hollowed areas completely enclosed within the external geometry of the bladelet. A solid line across the longitudinal direction of the bladelet was left intact after the optimization analysis, resulting in an internal feature similar to a stiffener.
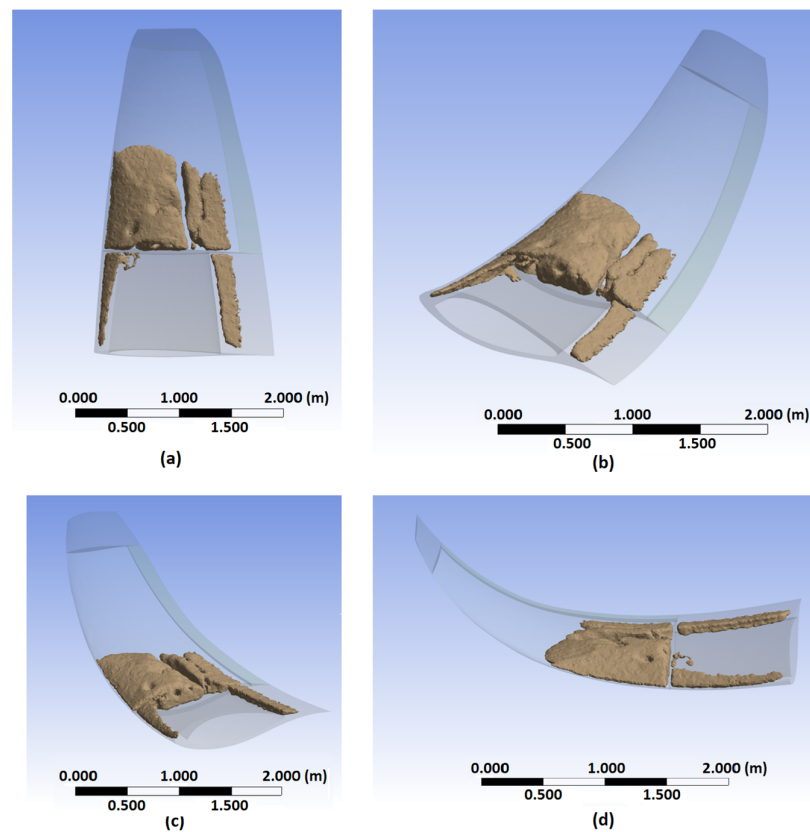
Figure 11. Interior material removal schematic via TO. (**a**) Top view, (**b**) isometric back view, (**c**) isometric front view, (**d**) front view.

An initial structural simulation was performed before the optimization analysis in order to assess the performance of the bladelet under operating conditions. After the finalization of the TO process an additional simulation was performed under the same conditions, utilizing the updated geometry to validate the procedure's results.

In Figure 12 the generated stress profiles can be observed before and after the optimization operation, taking into consideration the equivalent Von Mises average stress in each case. Whereas the overall distribution of mechanical stresses in both cases are very similar, a few minor differences can be observed around the middle area of the blade, suggesting that the removal of the material resulted in a minor increase of the concentrated stress in that area. This statement is further endorsed by the quantified data on both studies. Before material reduction the average stress generated on the component was calculated at 1.817 MPa. Post optimization this value increased to 2.69 MPa, exhibiting a 32% rise. Although this percentage signifies a considerable difference, the average values are very low compared to the mechanical strength of the part, taking into consideration the mechanical properties of the selected 3D printing resin, which presents an ultimate tensile strength of 80 MPa. Furthermore, the maximum calculated stress values exhibited an increase of only 5%, rising from 31.05 MPa to 31.68 MPa. This maximum value was observed on the trailing edge of the base of the bladelet, away from the areas where the shape alterations due to the optimization analysis occurred, suggesting that this difference could be within the margins of a computational error.
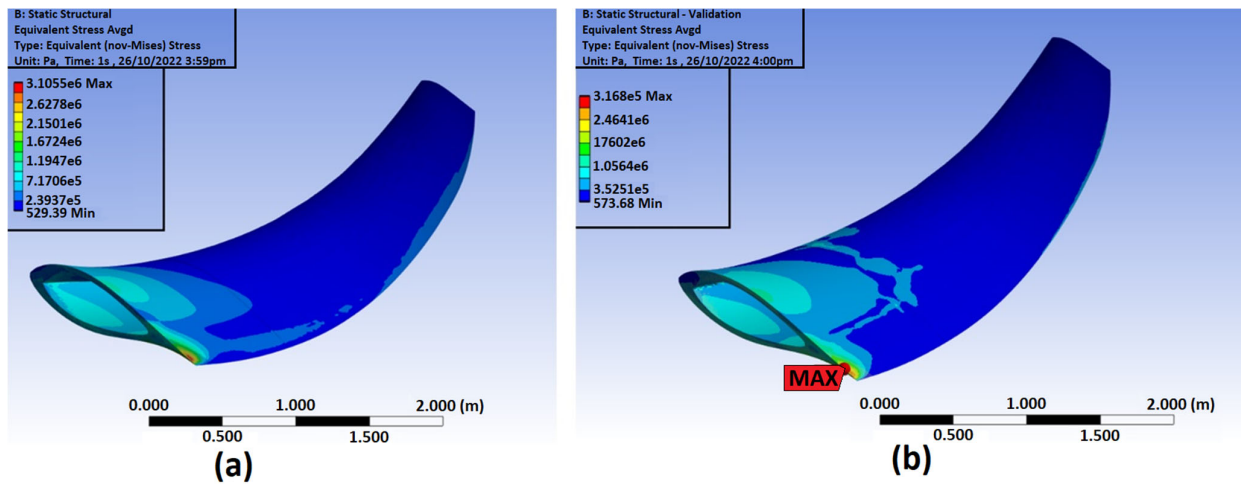
Figure 12. Comparative stress colormap. (**a**) Before TO, (**b**) after TO.

In Figure 13 the total deformation values are depicted, further supporting the similarity of the two cases. The deflection profiles are very similar, with the optimized variant actually exhibiting marginally smaller strain near its base. The average deformation before the optimization cycles was calculated at 1.04 mm whereas post optimization this value was raised up to 1.38 mm. While the relative increase appears to be high, reaching 24%, the values remain considerably low, in the order of millimeters. In terms of maximum deformation values, appearing on the trailing edge at the tip of the bladelet, the difference is even higher, increasing from 2.65 mm to 3.59 mm, a 26% increase with the values remaining significantly minimal. The safety factor in both cases was approximately 2.66, remaining above the set limit of 2.
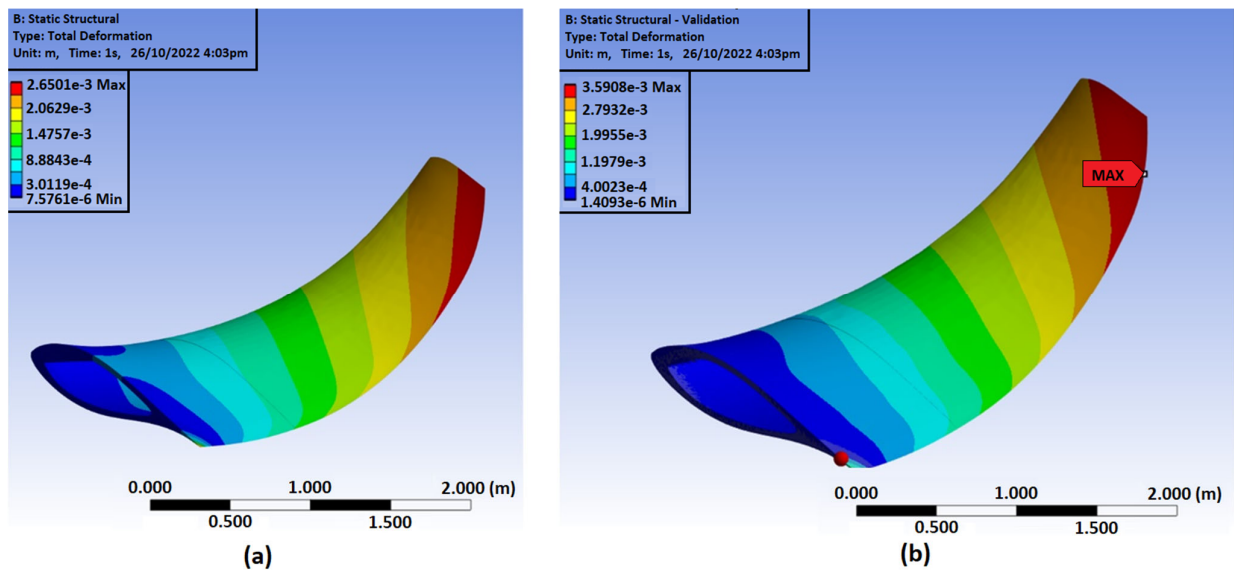

Figure 13. Comparative deformation color map. (**a**) Before TO, (**b**) after TO.

It is quite evident from the comparative charts presented above that, while the mass of the optimized component successfully met the reduction goals, the mechanical performance of the part did appear to present enhancement, though it remained within a relatively safe margin. Furthermore, the calculated values suggest that further optimization could be investigated by increasing the allowed material removal percentages. No further analysis will be performed nonetheless as excessive material reduction is expected to result in very thin geometries that should potentially raise fabrication issues.

3.3. Additive Manufacturing

Regarding the fabrication of the optimized bladelet prototype, the internal cavities formed during the TO process appear to be normally manufacturable using the selected Vat Photopolymerization 3D printing technology, with no further operations required to ensure fabricability. No internal support structures that would hinder the overall weight reduction benefit were required. A number of drainage orifices, as stated above, were necessarily implemented to ensure that no liquid resin remained trapped within the cavities after printing, as remaining amounts of resin inside the printed part would inherently lead to a weight increase and appearance of dynamic phenomena during the operation of the wind turbine prototype due to the liquid phase of the enclosed residue. An indicative representation of the draining orifices, marked with red color, connecting the internal hollow regions with the exterior area of the blade, can be seen on Figure 14. The exact number and form of the holes is case dependent during the 3D printing preparation stage, taking into account the orientation of the part and with consideration not to interfere with the components' performance.
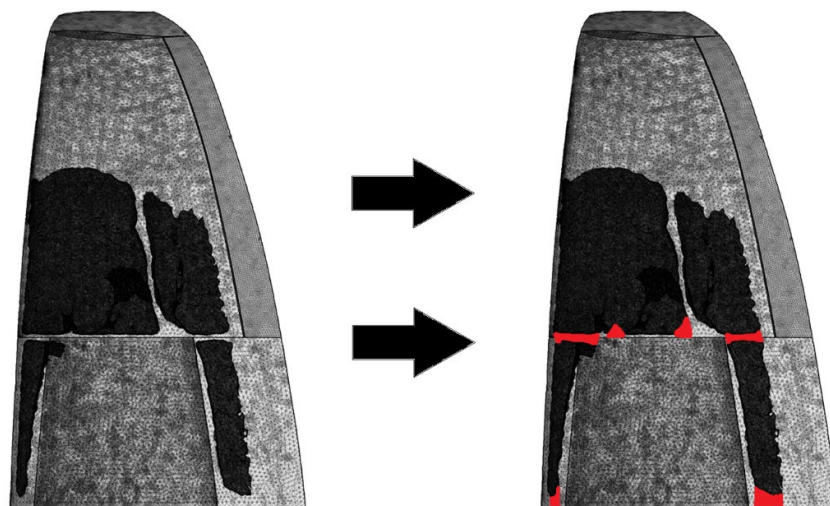

Figure 14. Indicative resin drainage scheme. Dark areas indicate hollow internal structure. Red markings indicate areas where further material removal is required for liquid resin drainage after 3D printing.

In order to ensure one-off production of the printed components, proper orientation on the build plate was required. Several test prototypes were placed diagonally, with the trailing edge facing upwards in a support-free orientation scheme, as the low thickness of the trailing edge in combination with the brittleness of the material would result in fractures around the edge. A 100 μm layer height was selected to balance fabrication quality and time, resulting in an 11-h printing process. Considering support structure profiles and printing profiles the default slicer options set by the original equipment manufacturer (OEM) were utilized. An indicative fabricated prototype is depicted in Figure 15.
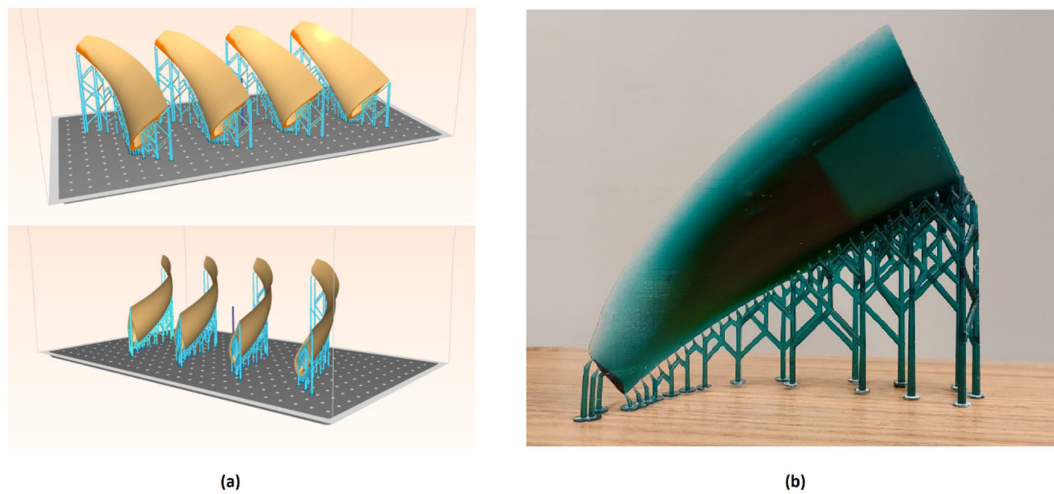
Figure 15. Model preparation and 3D printing. (**a**) Isometric slicer views, (**b**) 3D printed scaled down bladelet prototype (scale 1:20).

4. Conclusions

In this paper, a methodology for the two-stage optimization of a curved bladelet at the tip of a wind turbine blade is presented. An iterative shape optimization procedure was carried out to improve the aerodynamic properties of the added component, yielding an enhanced version of the original bladelet with approximately 30% increased generated torque on the bladelet itself and an overall 0.81% increase on the whole blade. A structural topology optimization workflow was further parameterized and utilized to reduce the weight of the bladelet, resulting in a 30% lighter part with similar mechanical properties to the original blade tip. The combined workflows resulted in a more lightweight component with higher cost efficiency due to reduced material consumption and increased performance with minor geometry alterations without detrimental impacts to the initial fabrication costs. An Additive Manufacturing approach was considered for the fabrication of the prototype of the bladelet allowed for further design flexibility during the parameterization of the optimization solver by facilitating the realization of complex internal organic features produced by the algorithms. The scaled-down prototype will be assembled under further physical experimentation to validate the simulated properties Further investigation regarding varying optimization parameters could potentially yield even more beneficial results.

References

1. Global Wind Report 2022. Available online: https://gwec.net/global-wind-report-2022/ (accessed on 10 October 2022).
2. Elia, A.; Taylor, M.; Gallachóir, B.Ó.; Rogan, F. Wind turbine cost reduction: A detailed bottom-up analysis of innovation drivers. *Energy Policy* **2020**, *147*, 111912. [CrossRef]
3. Brøndsted, P.; Nijssen, R.P. *Advances in Wind Turbine Blade Design and Materials*; Woodhead Publishing: Oxford, UK, 2013.
4. Plocher, J.; Panesar, A. Review on design and structural optimisation in additive manufacturing: Towards next-generation lightweight structures. *Mater. Des.* **2019**, *183*, 108164. [CrossRef]
5. Bhandari, R.; Kumar, B.; Mayer, F. Life cycle greenhouse gas emission from wind farms in reference to turbine sizes and capacity factors. *J. Clean. Prod.* **2020**, *277*, 123385. [CrossRef]
6. Scott, S.; Greaves, P.; Macquart, T.; Pirrera, A. Comparison of blade optimisation strategies for the IEA 15MW reference turbine. *J. Phys. Conf. Ser.* **2022**, *2265*, 032029. [CrossRef]
7. Reddy, S.R.; Dulikravich, G.S.; Sobieczky, H.; Gonzalez, M. Bladelets—Winglets on Blades of Wind Turbines: A Multiobjective Design Optimization Study. *J. Sol. Energy Eng.* **2019**, *141*, 061003. [CrossRef]
8. Sørensen, N.N.; Johansen, J. *Aerodynamic Investigation on Winglets on Wind Turbine Blades Using CFD*; Risø DTU—National Laboratory for Sustainable Energy: Roskilde, Denmark, 2006.
9. Peter, J. *Innovation in Wind Turbine Design*; Wiley: New York, NY, USA, 2018.
10. Mourad, M.G.; Shahin, I.; Ayad, S.S.; Abdellatif, O.E.; Mekhail, T.A. Effect of winglet geometry on horizontal axis wind turbine performance. *Eng. Rep.* **2020**, *2*, e1210. [CrossRef]
11. Reddy, S.R.; Sobieczky, H.; Dulikravic, G.S.; Abdoli, A. Multi-Element Winglets: Multi-Objective Optimization of Aerodynamic Shapes. *J. Aircr.* **2016**, *53*, 992–1000. [CrossRef]
12. Walker, D.; Liu, D. Topology Optimization of an Aircraft Wing. In Proceedings of the 56th AIAA/ASCE/AHS/ASC Structures, Structural Dynamics, and Materials Conference, Kissimmee, FL, USA, 5–9 January 2015.
13. Barnes, R.H.; Morozov, E.V. Structural optimisation of composite wind turbine blade structures with variations of internal geometry configuration. *Compos. Struct.* **2016**, *152*, 158–167. [CrossRef]
14. Zhu, J.; Zhou, H.; Wang, C.; Zhou, L.; Yuan, S.; Zhang, W. A review of topology optimization for additive manufacturing: Status and challenges. *Chin. J. Aeronaut.* **2021**, *34*, 91–110. [CrossRef]
15. Sessarego, M.; Feng, J.; Ramos-García, N.; Horcas, S.G. Design optimization of a curved wind turbine blade using neural networks and an aero-elastic vortex method under turbulent inflow. *Renew. Energy* **2020**, *146*, 1524–1535. [CrossRef]
16. Madsen, M.H.A.; Zahle, F.; Horcas, S.G.; Barlas, T.; Sørensen, N.N. CFD-based curved tip shape design for wind turbine blades: Design methods, reliability and uncertainty modelling. *Wind Energy Sci.* **2022**, *7*, 1471–1501. [CrossRef]
17. Dhert, T.; Ashuri, T.; Martins, J.R.R.A. Aerodynamic shape optimization of wind turbine blades using a Reynolds-averaged Navier-Stokes model and an adjoint method: Aerodynamic shape optimization of wind turbine blades. *Wind Energy* **2017**, *20*, 909–926. [CrossRef]
18. Tsiakas, K.T.; Trompoukis, X.S.; Asouti, V.G.; Giannakoglou, K.C. Shape Optimization of Wind Turbine Blades Using the Continuous Adjoint Method and Volumetric NURBS on a GPU Cluster. In *Advances in Evolutionary and Deterministic Methods for Design, Optimization and Control in Engineering and Sciences*; Springer International Publishing: Cham, Switzerland, 2019; pp. 131–144.
19. Ansys Blog. How Fluid-Structure Interaction Works and Why it's Important. 1 March 2022. Available online: https://www.ansys.com/blog/fluid-structure-interaction-explained (accessed on 15 October 2022).
20. Pollini, N.; Lavan, O.; Amir, O. Adjoint sensitivity analysis and optimization of hysteretic dynamic systems with nonlinear viscous dampers. *Struct. Multidiscip. Optim.* **2018**, *57*, 2273–2289. [CrossRef]
21. Kelecy, F.J.; Adjoint Shape Optimization for Aerospace Applications. Advanced Modeling & Simulation (AMS) Seminar Series. 8 April 2021. Available online: https://www.nas.nasa.gov/assets/nas/pdf/ams/2021/AMS_20210408_Kelecy.pdf (accessed on 1 July 2022).
22. Schaffarczyk, P. *Introduction to Wind Turbine Aerodynamics*; Springer: Berlin/Heidelberg, Germany, 2014.
23. Zhang, W.; Zhu, J.; Gao, T. *Topology Optimization in Engineering Structure Design*; ISTE Press Ltd.: London, UK; Elsevier Ltd.: Oxford, UK, 2016.
24. Zhao, J.; Wang, C. Dynamic response topology optimization in the time domain using model reduction method. *Struct. Multidiscip. Optim.* **2016**, *53*, 101–114. [CrossRef]
25. Bendsøe, M.P. Optimal shape design as a material distribution problem. *Struct. Optim.* **1989**, *1*, 193–202. [CrossRef]
26. Kandemir, V.; Dogan, O.; Yaman, U. Topology optimization of 2.5D parts using the SIMP method with a variable thickness approach. *Procedia Manuf.* **2018**, *17*, 29–36. [CrossRef]
27. Ferrer, A. SIMP-ALL: A generalized SIMP method based on the topological derivative concept. *Int. J. Numer. Methods Eng.* **2019**, *120*, 361–381. [CrossRef]
28. Bendsøe, M.P.; Singmund, O. *Topology Optimization*; Springer: Berlin/Heidelberg, Germany, 2004.
29. Posner, B.; Keller, A.; Binz, H.; Roth, D. Holistic lightweight design for function and mass: A framework for the function mass analysis. In Proceedings of the International Design Conference—DESIGN 2012, Dubrovnik, Croatia, 21–24 May 2012.

30. Michailidis, G. Manufacturing Constraints and Multi-Phase Shape and Topology Optimization via a Level-Set Method. Ph.D. Thesis, Ecole Polytechnique X, Palaiseau, France, 2014.
31. Lachouette, D.; Conraux, P.; Allaire, G.; Jouve, F. TOPOLEV:Topological. In *13e Colloque National en Calcul des Structures*; Université Paris: Paris, France, 2017.